JOURNAL OF GEOPHYSICAL RESEARCH, VOL. 103, NO. C4, PAGES 7857–7874, APRIL 15, 1998

Coastal wind field retrievals from ERS synthetic aperture radar images

Erik Korsbakken

Nansen Environmental and Remote Sensing Center, Solheimsviken, Bergen Norway

J. A. Johannessen

European Space Agency, European Space Research and Technology Centre, Noordwijk, The Netherlands

O. M. Johannessen

Nansen Environmental and Remote Sensing Center /Geophysical Institute, University of Bergen, Bergen, Norway

Abstract. A unique series of European Remote Sensing Satellite (ERS) 1 and 2 C band synthetic aperture radar (SAR) images was obtained off the southern coast of Norway during the Coast Watch'95 experiment in September 1995. In this paper we carry out a systematic analysis of the mesoscale coastal wind field conditions expressed in the SAR images. Four different categories of phenomena including windrows, fetch-limited seas, wind fronts, and oceanographic fronts are examined and discussed. The quantitative retrievals of the wind field are based on examination of both the SAR image backscatter characteristics and the spectral properties. Results are compared and validated against coincident ship and buoy data, providing complementary and independent observations of the oceanographic and meteorological conditions.

1. Introduction

Wind scatterometer observations over the ocean provide direct estimates of the global wind vector field at a spatial resolution of 50 km with an accuracy of ±2 m/s in speed, ±20° in direction and a directional ambiguity of 180° [*Stoffelen and Anderson*, 1993]. However, for some applications, such as in semi-enclosed seas, straits, coastal regions, estuaries, sea ice polynyas, and along the marginal ice zones, this resolution is too coarse. For monitoring and forecasting in these regions, wind field estimates retrieved from high-resolution synthetic aperture radar (SAR) images can therefore be very useful.

Quantitative estimates of the wind field from SAR images have not been systematically examined until recently. *Chapron et al.* [1995] have proposed a method for extracting the wind speed from the spectral properties of a SAR image. *Vachon and Dobson* [1996] have systematically applied the C band model (CMOD4) [*Stoffelen and Anderson* 1993] to ERS SAR data and compared with in situ measurements to provide qualitative performance assessments. *Vachon and Dobson* [1996] obtained an accuracy better than 1.5 m/s (compared to in situ measurements) if the wind direction was known and corrections for the ERS-1 SAR analog to digital conversion (ADC) saturation were applied. *Scoon et al.* [1996] have compared wind speed obtained using CMOD4 on SAR images from the English Channel to those from synoptic weather maps and conclude that a proper ADC correction is necessary to obtain reliable wind speed estimates.

In order to better quantify SAR imaging of upper ocean and atmospheric boundary layer processes, an experiment, Coast Watch'95 [*Johannessen et al.*, 1996], was carried out off the southwest coast of Norway during September 1995 as a ERS-1 and ERS-2 tandem announcement of opportunity project. The tandem operation provided a unique SAR coverage of the experiment area consisting of 148 SAR images (frames). Along-track scanning radiometer (ATSR) and National Oceanic and Atmospheric Administration (NOAA) advanced very high resolution radiometer (AVHRR) data were also obtained during the experiment. In situ meteorological and oceanographic observations were provided from the research vessel (R/V) *Håkon Mosby* of the University of Bergen, and an advanced metocean buoy from the Naval Postgraduate School (NPS), Monterey. Digital transmission of near real-time analysis of the SAR data to the vessel was continuously used in the planning and execution of the field study.

The main study objective reported in this paper is to optimize the wind retrieval from SAR by combinations of the two methods suggested above. We emphasize that our intention is not to improve the methods themselves, but to examine their responses under different conditions and taking advantage of combining the methods to derive the wind direction. We also want to compare the different algorithms against Coast Watch'95 in situ measurements and a meteorological hindcast model.

Because of the spatial resolution of the hindcast data as provided from the Norwegian Meteorological Institute, a direct validation based on these data becomes difficult, but the data are still used as an indication of the wind direction. The model is run on a 75 km resolution and based on a large number of in situ observations. Results are stored for off-line use with an interval of 6 hours.

In our analysis we use the procedure outlined by *Korsbakken* [1996] and *Korsbakken and Johannessen* [1996], and section 2 contains a brief review of the two retrieval methods. Application of the methods to the Coast

Paper number 97JC02580.
0148-0227/98/97JC-02580$09.00

Watch'95 data is reported in section 3 including a systematic comparison of the separate wind speed estimates from the spectral and radar backscatter properties (CMOD4) of the SAR images as well as a combination of the two methods. Three different categories of wind regimes are used, and in section 4 the results are discussed in accordance with the characteristics of these different regimes.

In particular, we present a comparison of the wind speed results, in areas where we do not have supporting ground truth, motivated by the following.

1. We believe that there are basically two different mechanisms responsible for the wind speed response in the two methods, namely, the short centimeter-scale waves for the CMOD4 and the longer wind-generated waves for the azimuth cutoff method. This makes it interesting to compare the two different algorithms under different conditions.
2. Consistency in the derived wind speed results is important for the method to obtain the wind direction.
3. Comparisons to local in situ measurements are not satisfactory to validate these algorithms to obtain a high spatial resolution wind field for a larger area (of course, limited by the SAR coverage).
4. Different responses in the methods may provide new oceanic information.
5. We want to demonstrate local variability, especially in coastal regions.

Finally, in section 5 the main results including the feasibility of the methods are summarized.

2. Wind Retrieval Algorithms

The two SAR wind retrieval algorithms are based on the extraction of the wind field from different parts of the ocean surface wave spectrum, in particular the medium wind-wave regime and the small centimeter-scale regime. Figure 1 shows a conceptual overview of the wind field estimation described below.

2.1. SAR Wind Algorithm

The SAR wind algorithm (SWA; the notation is used for the first time in this paper), proposed by *Vachon et al.* [1994] and further examined by *Chapron et al.* [1995], is based on a relation between the smearing effects [*Hasselmann and Shemdin* 1982] in the SAR image and the wind field. Smearing effects tend to increase the coherence (correlation) length of the radar returns in the spatial image domain and to influence the spectral properties of the SAR image.

The SWA is derived from a comparison of ERS SAR wave-mode data and the ERS wind scatterometer data which can be simultaneously acquired with the same satellite. In the case of a fully developed sea (no fetch limitation), the empirical SWA relation, based on an evaluation of 1200 SAR wave-mode imagettes with a central incidence angle of 20.2°, is given by *Chapron et al.* [1995] as

$$U_{10} = 4.75\left(\frac{\lambda_c - 30}{110}\right) \quad \mathrm{m\ s^{-1}} \qquad (1)$$

where U_{10} is the wind speed at 10 m above the surface and λ_c is the azimuth cutoff wavelength.

Expression (1) is also consistent with the expression $\lambda_c = 23.4U_{10} + \Lambda$ as given by *Kerboal et al.* [this issue], who discuss the method and its capabilities in greater detail. In this expression Λ represents a residual cutoff involving the nominal SAR azimuth resolution. In case of the SAR precision image (SAR.PRI) as used in this study, the nominal azimuth resolution is about 30 m (Λ = 30 m).

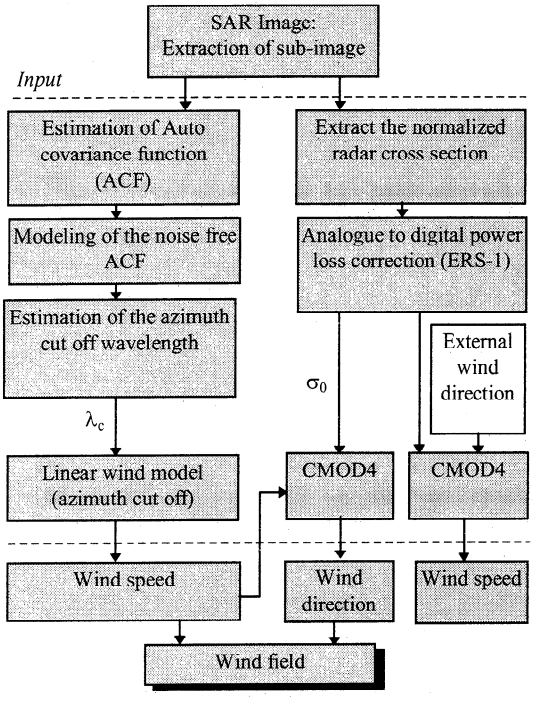

Figure 1. Conceptual overview of wind retrieval models. The external wind direction may be obtained from windrows in the SAR image as proposed in the text.

Assuming a Gaussian shaped low-pass filter for the azimuth cutoff, the cutoff wavelength can be estimated from the autocovariance function (ACF) derived from an inverse Fourier transform of the SAR image power spectrum (the Wiener Khinchin theorem). The effect of strong azimuth filtering effects due to the smearing and, finally, the azimuth cutoff are clearly seen in the presentation of the case studies in this paper. As proposed by *Chapron et al.* [1995], the ACF can be regarded as a sum of the narrow peak due to the system response of the broadband noise and a broadened "shoulder" corresponding to the Gaussian-shaped filter (in the spectral domain) defined as $c(x)=\exp(-\pi x/\lambda_c)^2$, where x is the lag in the ACF. A Gaussian function $f(x)=\exp(-ax)^2$ is then fitted to the ACF in the azimuth direction over the broadened "shoulder" part of the function to determine a. In return, λ_c is then obtained from the relation $f(x)=c(x)$.

The spatial resolution of the SWA method is limited by the needed full-resolution subimage to obtain statistical confidence in the estimation of the SAR image power spectrum.

2.2. The CMOD4 Model

The CMOD4 wind retrieval model [*Stoffelen and Anderson* 1993] was developed for the ERS-1 C band scatterometer, but it has also been shown to give good estimates of wind speed when applied to ERS-1 SAR images [e.g. *Johannessen et al.*, 1995; *Vachon et al.*, 1995; *Vachon and Dobson* 1996; *Wackerman et al.*, 1996]. The CMOD4 model provides σ_0 values as a function of relative wind

direction (ϕ=0 for a wind blowing toward the radar), wind speed, and incidence angle, expressed as

$$\sigma_0 = B_0[1 + B_1 \cos(\phi) + B_2 \cos(2\phi)] \quad (2)$$

The coefficients B_0, B_1, and B_2 depend on the local incidence angle of the radar beam and wind speed. The accuracy in the model is ±20° in relative wind direction and ±2 m/s in wind speed when applied to scatterometer data.

The CMOD4 model is derived for a neutral stratification. In order to compute the wind speed (U_{10}) from the radar backscatter accounting for the stratification (ΔT) in the atmospheric boundary layer (ABL) the CMOD4-derived wind speed must be modified following the method suggested by *Wu* [1993] or *Smith* [1988].

The saturation effect of the ADC in the satellite is described by *Meadows and Willis* [1995], *Laur et al.* [1993], and *Scoon et al.* [1996]. The effect is strongest in the near range and increases with radar backscatter intensity (e.g. at medium to high winds over the ocean surface) and leads to an underestimation of σ_0, which has to be compensated in order to properly estimate the absolute value of the radar backscatter. In turn, underestimation of σ_0 leads to an underestimation of the wind speed.

In this work the absolute calibrated σ_0 from ERS SAR is derived in accordance with a comprehensive calibration scheme provided by European Space Agency (ESA) [*Laur et al.,* 1996] except for correction for variance in the replica pulse power. The latter is shown to be negligible using the CMOD4 algorithm for wind speed retrieval in SAR data [*Scoon et al.,* 1996].

In this paper we also emphasize that the wind direction can be estimated from the CMOD4 model for different incidence angles, provided the wind speed, derived from the SWA method, can be associated with the corresponding measured radar backscatter (σ_0). In such cases we will show that four solutions, i.e., two pairs, each with a 180° ambiguity can be found, except in the cases when the direction is close to upwind (the wind blowing toward the radar) or downwind, for which only one pair is found. (Note that for the three beam scatterometers on ERS-1 and ERS-2 the number of solutions is reduced to a single pair with a 180° ambiguity.)

It has also been demonstrated [*Johannessen et al.,* 1995] that windrows manifested in the SAR images can be used to indicate the near-surface wind direction during the SAR integration time. In such cases, the number of wind direction solution pairs is also reduced to one (180° ambiguity). In some cases, e.g., off-ice and offshore winds the ambiguity can be completely resolved. Estimating the wind direction has also been proposed derived from the long-wave part (1000 m or more) of the SAR image power spectrum [*Vachon and Dobson* 1996; *Wackerman et al.,* 1996]. This requires that that the spectra are estimated from subimages large enough to resolve the low-frequency part of the spectra and that the wind streak pattern appear as a stationary wave field within the subimage.

3. Coast Watch'95 Analysis

The analyzed SAR data is three-looks ground range data in ERS PRI format, which is corrected for antenna elevation gain and range spreading loss. The ground resolution in range (normal to the satellite track) direction and azimuth is about 30 m, and the pixel size is 12.5 m in each direction. All satellite passes are descending tracks, and here the northernmost SAR image is always referred to as the first. Each SAR image (100 × 100 km) has been regularly divided into 9 × 9 subimages covering about 10 × 10 km at the ground.

The SWA wind speed and SAR image power spectrum (SIPS) are estimated from each subimage following the method suggested by *Monaldo* [1991]. For the estimation of the CMOD4 wind speed and direction, each subimage is averaged to a pixel size of 100 × 100 m before the ERS-1 data are corrected for the ADC power loss according to *Laur et al.* [1996]. The CMOD4 wind speed is then calculated and compared to the SWA-derived wind speed assuming the in situ wind direction from the R/V *Håkon Mosby* to be valid in all subimages. The wind direction is also independently estimated from the CMOD4 model function by a combination of the SWA wind speed and the calibrated radar backscatter. The ambiguity in wind direction is then resolved by comparing the four results with the in situ measured wind direction and also the windrows seen in the SAR image.

Three case studies from the Coast Watch'95 database are presented, including case 1, windrows under fetch-limited conditions; case 2, wind front; and case 3, oceanic front (jet) together with a local wind front.

A composite overview of these three cases including the SAR image expressions together with the retrieved wind vector maps is shown in Figures 2-5. They can be briefly characterized as follows.

Case 1 includes the ERS-1 SAR images from September 16, 1995 (Figure 2, left), which show a very characteristic pattern of windrows aligned in the wind direction of about 120°. There is also a gradual increase in the backscatter toward the south. The corresponding wind vector map is shown in Figure 2 (right). The wind speed in the vicinity of the ship is about 13 m/s and reveals a clear northwest gradient, as expected.

The SAR images from September 17, 1995 (Figure 3, left), also show a pattern of windrows with an orientation of about 110° as well as higher backscatter in the southern parts. The corresponding wind vector map (Figure 3, right) confirms this. Overall, the wind speed has dropped by about 4-5 m/s in comparison to the previous image.

Case 2 includes the SAR images from September 23, 1995 (Figure 4, left), which show a characteristic local wind front appearing as a bright-dark boundary. Windrows are also present. The corresponding wind vector map shows a northeasterly wind speed gradient and a wind direction of 260-300°.

Case 3 the final case study, is based on the SAR images from September 27, 1995 (Figure 5, left), which shows a westward flowing coastal jet bounded by two distinct, and in some places parallel fronts. A local, 5-10 km wide wind feature is also running diagonally, in the second image. The corresponding wind vector map (Figure 5, right) shows a wind speed of about 10 m/s from the southwest at about 215°.

A more detailed analysis of the three cases is presented systematically below. Since many of the SAR images express distinct areas associated with the different surface conditions, they are divided into subareas to ensure near-homogeneous backscatter within the analyzed subimages. A selection of the SIPS as obtained within the different regions of the image is

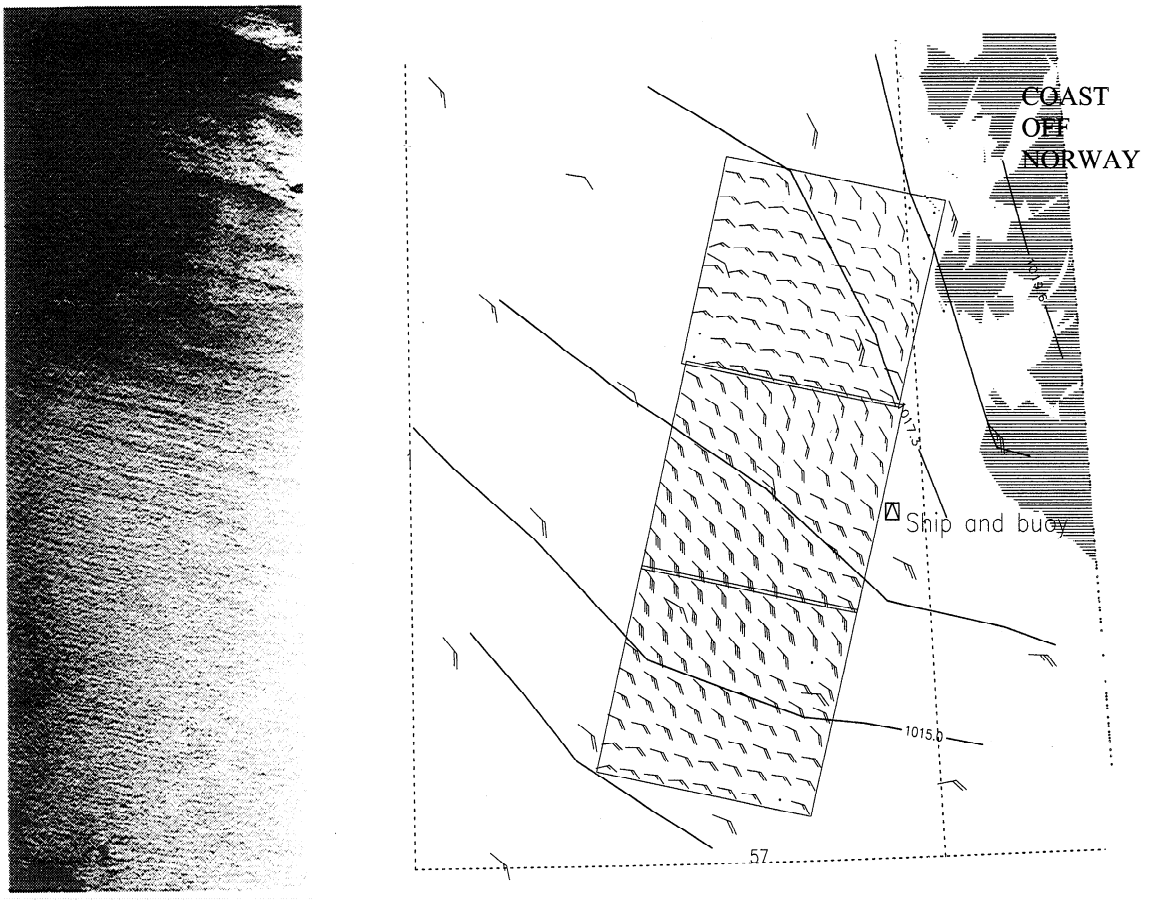

Figure 2. Case 1: SAR images from September16 (left) and corresponding wind vector map derived from inverting the CMOD4 model function using the SWA wind speed and the calibrated bakscatter (right). Isobars and corresponding surface wind vectors from diagnostics are superimposed. The position of the R/V *Håkon Mosby* and the "metocean" buoy at the satellite overpass is indicated. The observed discontinuity in wind direction between the northernmost and the center image is due to the processing of the SAR images as discussed in the text.

also plotted to demonstrate the effects of variability in the wind speed from one subarea to another for case 2 and 3. The SIPS do not provide direct quantitative information about the real sea state, but they are still valid in assessing the SWA performance, since the wind information is directly derived from the azimuth response in the spectra. Moreover, if we assume a linear ocean to SAR mapping of the ocean waves, the SIPS will still contain valuable information of the main wave modes and their propagation direction.

3.1. Case 1: Windrows (Fetch)

Four distinct subareas are identified in the composite of the three SAR images from September 16 as illustrated in Figure 6 (left). They include nearly homogeneous backscatter with no structure (area 1), low frequent streaks (area 2), homogeneous (periodic) wind streaks (area 3), and windrows with dark patches in between (area 4). Superimposed on the figure is the ship track.

In comparing the SWA and CMOD4 derived wind speed, about 80% of a total of 238 subimages have a wind speed difference less than 2 m/s using the in situ measured wind direction to present all subimages in the CMOD4 model. In the scatter plots in Figure 7 the wind speed ranges from 3 to 15 m/s. The correlation is good for areas 1 and 2, and the SWA wind speed retrievals tend to be higher than the CMOD4 wind speed for area 3, although some impression of saturation is seen in CMOD4 at winds around 9 m/s. For the low number of subimages in area 4, the correlation seems to be relatively good. Deviations in the obtained wind speeds will be further discussed in terms of surface conditions and spatial variability in section 4.

The second and third SAR image were originally processed using a nominal chirp function in the processing of the SAR image (information provided by ESA). Compared to standard processing, where the chirp function is extracted from the received raw SAR data, this leads to a reduction in the average σ_0 value. To compensate for this, ESA provided a correction constant of 4.1 dB to be added. This correction may not preserve the full dynamical range of backscatter and may cause the saturation-like effect in area 3. Similarly, a discontinuity in the derived wind direction is seen in Figure 2; on the other hand, this is not supposed to impact on the SWA wind speed. Nonetheless, the wind direction retrieved from the combination of SWA and CMOD4, as shown in Figure 2, is in good agreement with the observed windrows in the SAR images as well as the in situ measurements.

Table 1 summarizes the observations in areas 1 to 4, listing the main properties of the subareas and the corresponding

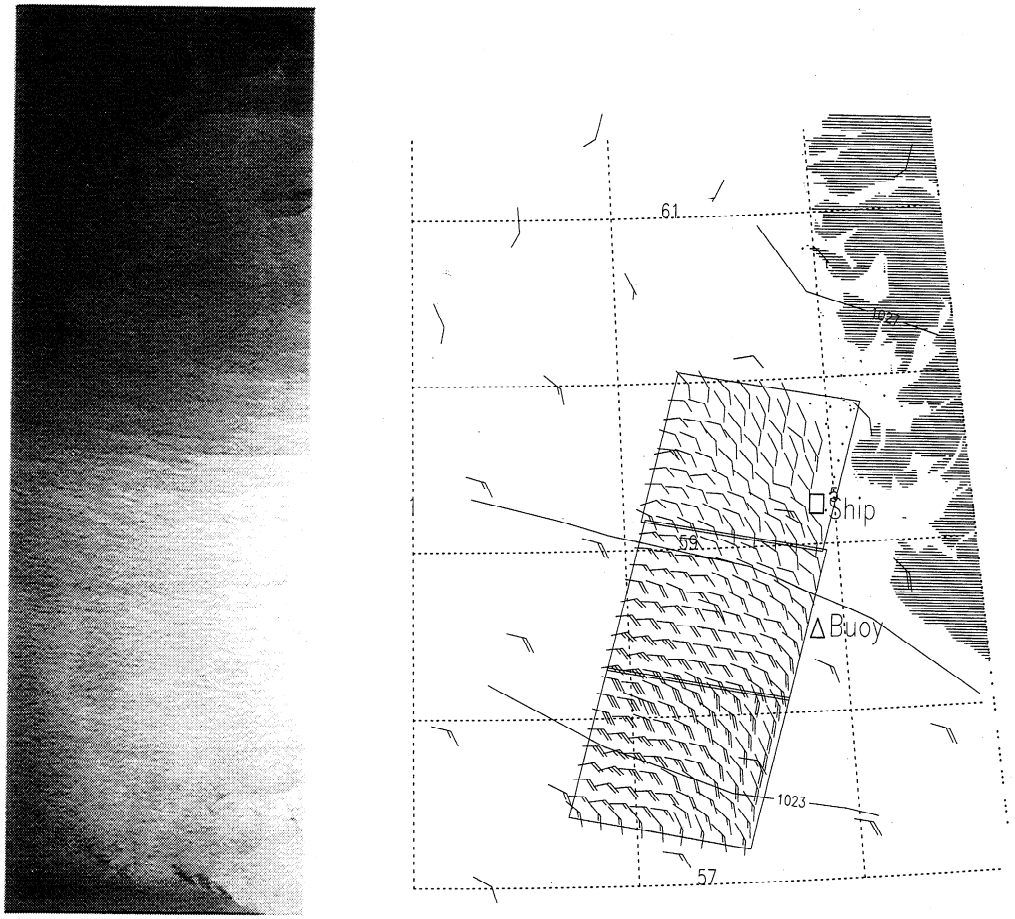

Figure 3. Case 1: SAR images from September 17 (left) and corresponding wind vector map derived from inverting the CMOD4 model function using the SWA wind speed and the calibrated backscatter (right). Isobars and corresponding surface wind vectors from diagnostics are superimposed. The positions of the R/V *Håkon Mosby* and the "metocean" buoy at the satellite overpass are indicated.

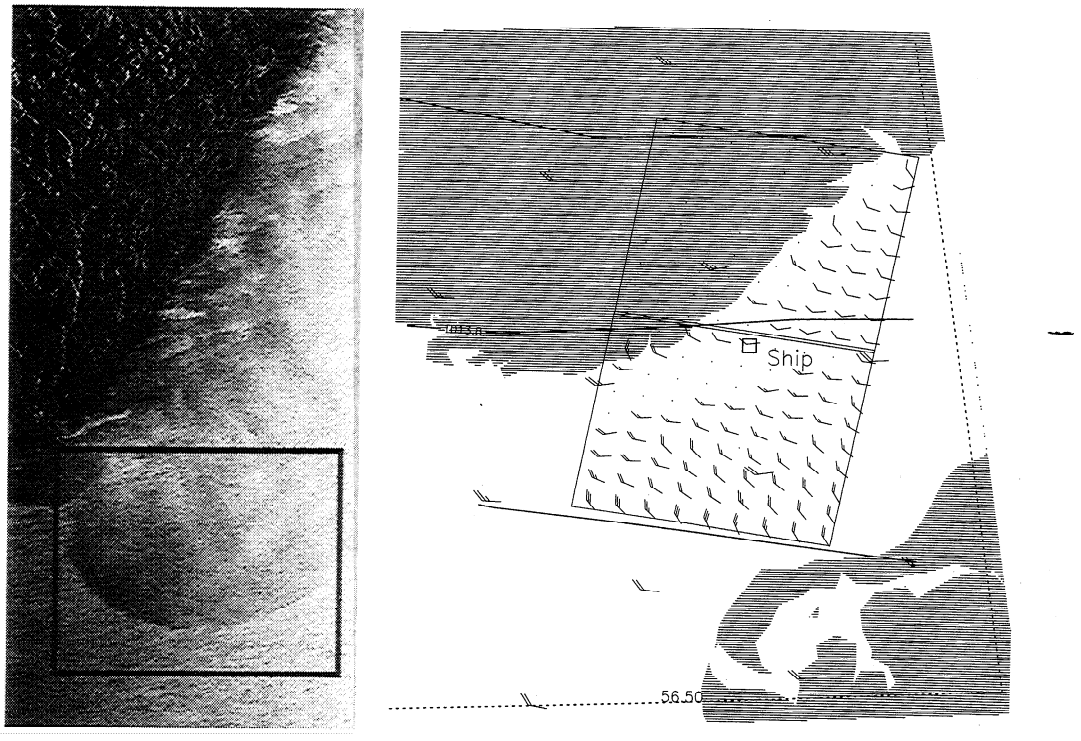

Figure 4. Case 2: SAR images from September 23 (left) and corresponding wind vector map derived from inverting the CMOD4 model function using the SWA wind speed and the calibrated bakscatter (right). Isobars and corresponding surface wind vectors from diagnostics are superimposed. The positions of the R/V *Håkon Mosby* at the satellite overpass is indicated. Boxed area indicated in the SAR image is a subimage used in Figure 12.

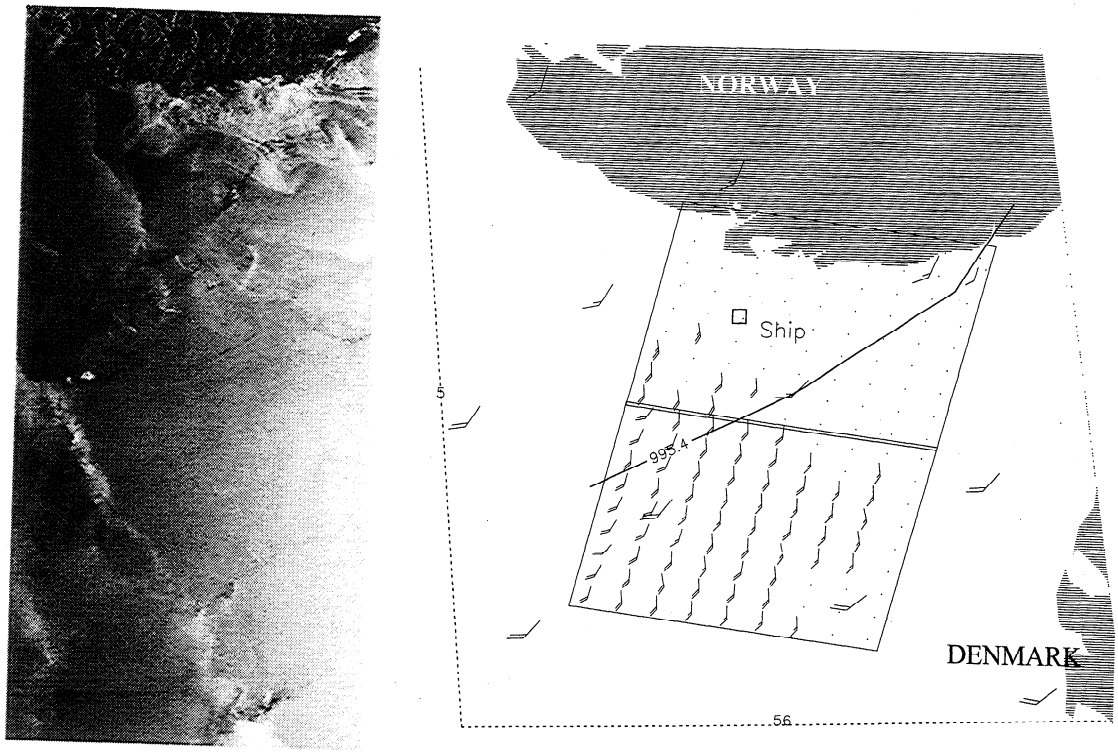

Figure 5. Case 3: SAR images from September 27 (left) and corresponding wind vector map derived from inverting the CMOD4 model function using the SWA wind speed and the calibrated backscatter (right). Isobars and corresponding surface wind vectors from diagnostics are superimposed. The position of R/V Håkon Mosby at satellite overpass is indicated.

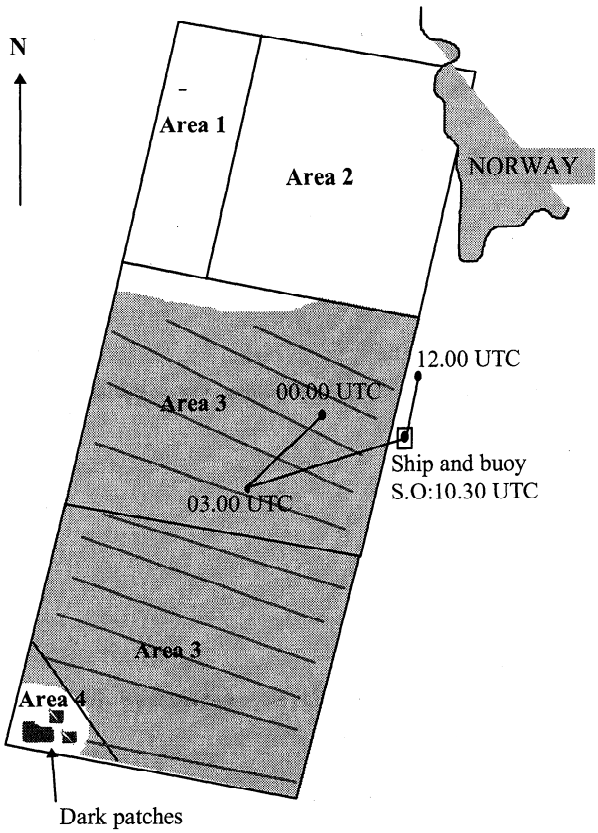

Figure 6. Identification of subareas of the SAR images on September 16, 1995 (left) together with the ship track prior to and during satellite overpass. Shaded area marks the presence of windrows and the lines roughly indicate the orientation but not the spacing of the windrows. The ship and buoy were in the same position at satellite overpass as marked by S.O.

SAR image power spectra as extracted from the subareas, and finally, the difference in the derived SWA and CMOD4 wind speeds and wind directions from the combination of SWA and CMOD4 provided collocated with wind direction from the hindcast model and in situ observation if available. Because of the spatial resolution of the hindcast model of 75 km the number of collocated data sets become limited.

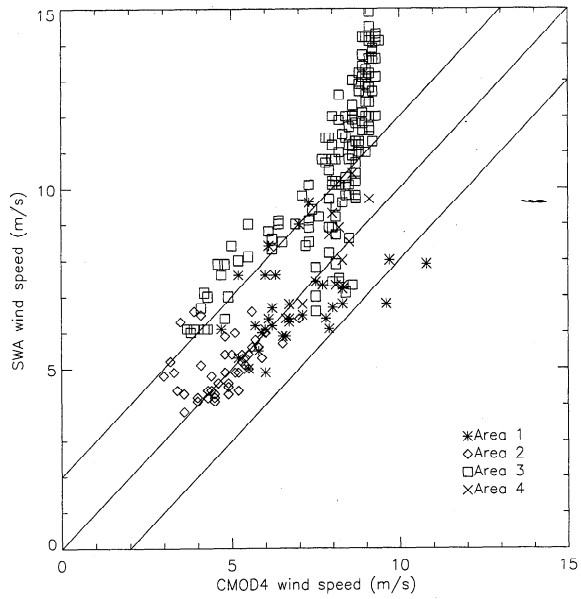

Figure 7. CMOD4 wind speed versus SWA wind speed derived from the SAR images on September 16, 1995. The interval of ±2 m/s is indicated.

Table 1. Summary of Analyses of September 16 SAR Images

Area Location (SAR Images 1,2, and 3, From Top to Bottom in Figures 2 and 6)	Features Observed in the Different Areas	Waves Obtained From SIPS	SWA-CMOD4 Wind Speed Comparison (Magnitude of Difference in the Area)	Wind Direction		
				SWA Combined With CMOD4	Hindcast	In Situ
Area 1, westernmost part of the first image	Nearly homogeneous, no presence of streaks	Mode of about 300 m propagating 45° to range direction	CMOD4>SWA (7 - 3 m/s)	84°	114°	
Area 2, main part of the first image	Streaks which are more low frequent than the characteristic windrows	Mode about 500 m propagating about 20° to range direction	CMOD4~SWA (1 - 2 m/s)	105°	152°	
Area 3, the second and third image	Characteristic homogeneous windrows	A strong mode of about 100 m in near range direction and a long mode (>300 m) in near azimuth direction	CMOD4<SWA (0 - 2 m/s)	125° 136°	124° 114°	130°
Area 4, lower south-east parts of the third image	Characteristic windrows and some dark spots	A strong mode of about 100 m near 45° to range direction and a long mode (>300 m) in near azimuth direction	CMOD4>SWA (2 - 4 m/s)	96°	123°	

In order to validate the wind field estimates further, these results are compared to meteorological records (obtained by the R/V *Håkon Mosby* along the ship track) prior to and at the satellite the overpass (see Table 5). The wind speed shows fluctuations between 10 and 13 m/s before the satellite overpass, while the wind direction was stable at 120° prior to the satellite overpass. Very good agreement between the wind direction along the ship track and the observed windrows in the SAR image is found, suggesting that the use of the in situ direction in all CMOD4 estimates is valid. The air-sea temperature difference shows only a weak unstable (ΔT=-1°C) atmospheric boundary layer stratification at the satellite overpass, allowing us to neglect this in the CMOD4-SWA comparison.

Another SAR image with clear expressions of windrows is obtained for exactly the same area 1 day later on September 17 (Figure 3). Three distinct areas are identified in this SAR image, as shown in Figure 8 (left). Again, the northernmost area, west of the coast, lacks expression features, while in the southern areas are windrows with a west-northwestward orientation of 110°.

Wind retrievals from a total of 238 subimages were compared for the September 17 images. The CMOD4 - SWA wind speed difference was less than 2 m/s for about 90% of the subimages. The scatter plot in Figure 9 reveals good agreement between the SWA and the CMOD4 derived wind speeds in the range of 3 to 15 m/s for all three images. In contrast to the previous results, no evidence of saturation is found for the high CMOD4 winds in this case. The outliers in area 1 (represented in Figure 9 as squares) arise from a very dark patch (low σ_0) close to the coastline where the SWA wind retrieval method fails because of fetch-limited seas with

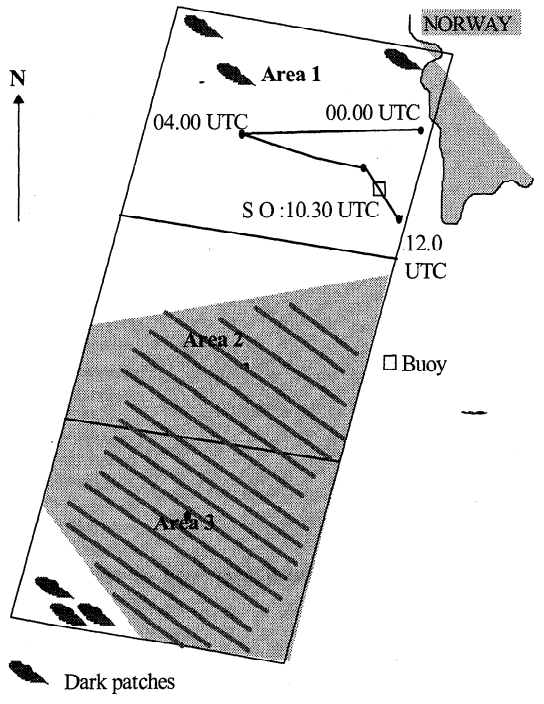

Figure 8. Identification of subareas of the SAR images on September 17, 1995 (left) together with the ship track prior to and during satellite overpass. Shaded marks presence of windrows and the lines roughly indicate the orientation but not the spacing of the windrows. The ship position at satellite overpass is marked by S.O.

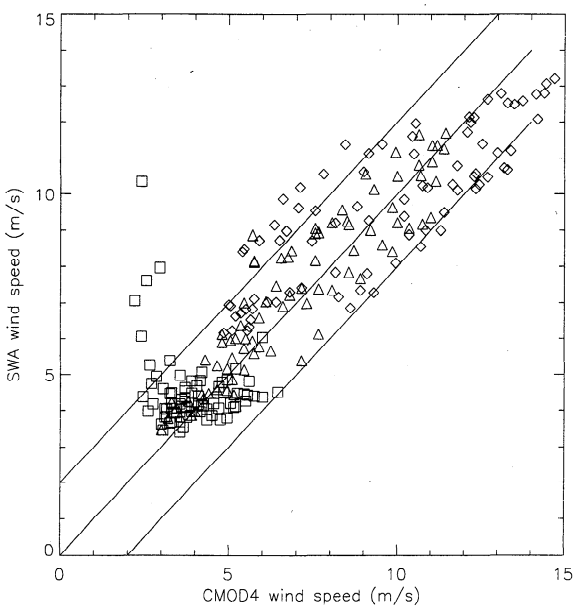

Figure 9. CMOD4 wind speed versus SWA wind speed, derived from the SAR images on September 17, 1995. The interval of ±2 m/s is indicated. The subimages containing land are rejected. Squares are used for the northernmost SAR image, triangles for the center image, and diamonds for the southernmost SAR image.

subsequent lack of fully developed waves and corresponding wave modulation. In such regions, no particular azimuth cutoff is present, and the azimuthal resolution is only dependent on the response function of the system (speckle noise response), and the SWA method produces high wind speed values . Therefore no wind vectors could be produced in this area (see Figure 3), since there were no intersecting points between observed σ_0 and modeled σ_0 based on the SWA wind speeds.

There is generally very good agreement between the wind vector map and the isobars superimposed on the map (Figure 3) both in regard to direction and to changes in magnitude from north to south.

Table 2 summarizes the observations for the three areas including a listing of the main properties of the subareas and the corresponding SAR image power spectra as extracted from the sub-areas and, finally, the response in the derived wind speeds and wind directions.

Although the range of winds in the September 16 to 17 SAR images is about the same, there is a gradual decrease in wind speed at the buoy and ship locations. This explains why the wave field is undergoing moderate changes.

The meteorological records from the R/V *Håkon Mosby* in the time period before, during, and after the satellite overpass, show that the wind speed is gradually decaying in the area before the satellite overpass reaching about 7 m/s as mentioned above, while the wind direction was relatively stable at 100° prior to and at satellite overpass. The air-sea temperature difference is weak and slowly changing to neutral. A southward increase in the wind speed of about 4 m/s over the distance from the ship (6-7 m/s) to the buoy (10-11 m/s) is also encountered, in agreement with the SAR-derived wind vector map (Figure 3).

3.2. Case 2: Wind Front

The SAR images from September 23 display the existence of a clear wind front (Figures 4 and 10). The images have moreover been arranged into three areas (Figure 10, center), in which area 1 is in the near-shore zone, area 2 is immediately north of the wind front, and area 3 is out of the front. Weak

Table 2. Summary of Analyses of September 17 SAR Images

Area Location (SAR Images 1,2, and 3, From Top to Bottom in Figures 3 and 8)	Features Observed in the Different Areas	Waves Obtained From SIPS	SWA-CMOD4 Wind Speed Comparison (Magnitude of Difference in the Area)	Wind Direction		
				SWA Combined With CMOD4	Hindcast	In Situ
Area 1 (Image 1)	Dark patches	Weak range traveling mode at about 100 m	CMOD4 > SWA (0 to 1 m/s)	98°	124°	—
				108°	147°	
Area 2 (Image 2)	Windrows	Strong short mode of about 100 m 20° to range and a near azimuth traveling mode at about 500 m	SWA > CMOD4 (0 to 1 m/s)	101°	124°	100°
Area 3 (Image 3)	Windrows and some dark patches in low left corner	Short mode of about 100 m 20° to range and a near azimuth traveling mode at about 500 m	SWA > CMOD4 (0 to 1 m/s)	100°	107°	
				87°	96°	
				140 °	101°	

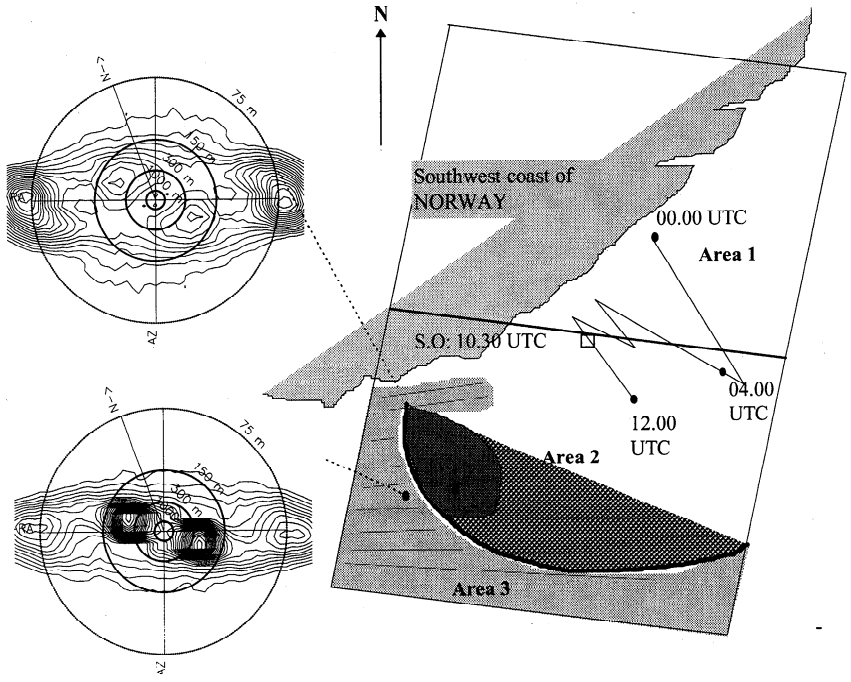

Figure 10. Identification of subareas of the SAR images on September 23, 1995 (center) together with the ship track prior to and during satellite overpass. Shaded area marks the presence of windrows, and the lines roughly indicate the orientation but not the spacing of the windrows. The ship position at satellite overpass is marked S.O. A selection of SAR image power spectra in the different areas (left). The concentric circles indicate wavelengths of 1000 m (inner ring), 300, 150, and 75 m, RA is range direction, AZ is azimuth direction, and N is north.

evidence of windrows is found in areas 2 and 3. Superimposed on the figure is the ship track, while the locations and extracts of the SAR image power spectra are shown to the left.

The wind front curves through the image with a width or transition zone of about 15 to 20 km. The largest gradient in σ_0 appears to be oriented approximately perpendicular to the wind direction (darkest area in the front as illustrated in Figure 10), while the σ_0 gradient becomes weaker as the frontal orientation becomes more closely aligned with the wind direction. A pattern of northeast oriented windrows is seen in the upper left part of the second image between the front and the coastline. Some windrows are also manifested to the south of the front. The in situ wind direction indicates that the fetch distance should be more than 200 km in the second image, and fetch-limited seas are expected in the northwest sector, in area 1, of the first image.

A total of 116 subimages were examined, of which 60% have a SWA-CMOD4 wind speed difference of less than 2 m/s in the range from 3 to 15 m/s as shown in Figure 11. The SWA wind speed tends to be somewhat less than the CMOD4 wind speed in area 1. In area 2 the majority of the estimates are still within ±2 m/s, but we also observe that some of the CMOD4 wind speed estimates exceed the SWA wind by more than 2 m/s. However, in area 3 the agreement is generally poor, with the SWA wind speed generally larger (more than 2 m/s) than the CMOD4 wind speed. Possible reasons for the lack of agreement in this area may be due to incoming swell as derived from the SIPS analysis (Figure 10), which in turn, increases the SWA wind speed.

The change in the CMOD4 wind speed across the front from area 2 to 3 is about 2-3 m/s, as indicated in the contour plot (Figure 12) of the derived CMOD4 wind speed obtained using the in situ northeasterly wind direction of 220°.

The wind field derived from inverting the CMOD4 model function combined with the SWA wind speed and the calibrated σ_0 is shown in Figure 4, together with the hindcast isobaric map and wind vectors from the hindcast model 90

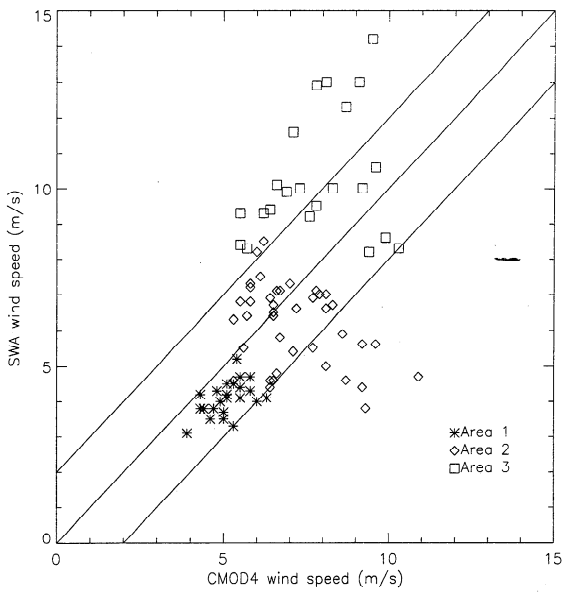

Figure 11. CMOD4 wind speed versus SWA wind speed derived from the SAR images on September 23, 1995, and classified according to the three areas. The interval of ±2 m/s is indicated.

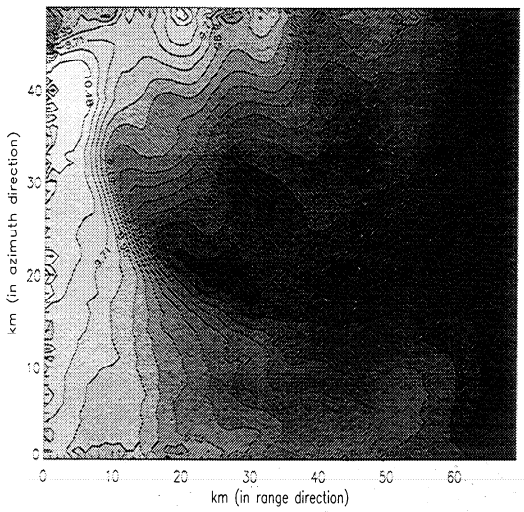

Figure 12. Contour plot of the CMOD4 wind. The structure reflects the change in wind speed across the front seen in the image. Also the local increase in wind close to the coast is clearly seen in the upper left part of the plot. The subimage frame is shown in Figure 4.

min after the satellite overpass. In area 2 a patch of windrows aligned with the in situ wind direction stretching along the coast and eastward in the top of the second image has no wind vectors which can be associated with diverging SWA and CMOD4 wind speeds. The presence of these windrows suggests that there may be a local increase in the wind speed in this area. This is also reflected in the CMOD4-derived wind speed (in area 2), which is about 2 m/s higher than the CMOD4 wind speed in the surrounding areas, whereas the SWA wind speed does not respond similarly. The increased CMOD4 wind speed is also seen in Figure 12 as a peak in the upper left part of the plot.

During the satellite overpass, the ship position was about 75 km northeast of the wind front. Prior to the overpass, the winds varied from 8 to 15 m/s, and at overpass the wind speed in the area of the R/V *Håkon Mosby* was about 12 m/s, while the wind direction remained constant around 250° during the observation time.

Unstable stratification of about 2°C slowly changing toward neutral is encountered along the ship track during the observation interval. This may help to explain why CMOD4 seems to overestimate the wind speed in area 3 (Figure 11).

Table 3 summarizes the observations for the three areas analyzed in case 2 including a brief characterization of areas, features, SIPS results and the derived SWA versus CMOD4 wind speed differences, as well as comparison of the wind direction retrievals.

3.3. Case 3: SST Oceanographic Front and Wind Front

As shown in the beginning of this section, the SAR images from September 27, 1995 (Figure 5, left) express a westward flowing coastal jet bounded by two distinct, and in some places parallel fronts as well as a narrow-banded diagonal wind feature with some backscatter patches possibly originating from rain showers and downdraft. In Figure 13 the SAR is shown to be classified into five distinct zones covering the vicinity of as well as inside these frontal features. Superimposed on the figure is the ship track and the locations and extracts of four SAR image power spectra.

A total of 144 subimages were analyzed for the September 27 image (Figures 5 and 13), of which only 8% have a wind speed difference of less than 2 m/s in the range from 3 to 15 m/s. Figure 14 shows that the SWA wind speed is up to 10 m/s higher than the CMOD4, in particular, for areas 2 and 3. A shift of about 1.5 m/s to 2 m/s in the CMOD4 wind speed is observed across the jet and across the wind front between areas 4 and 5, as seen in the left plot in the Figure 14. In contrast to CMOD4 wind speeds, there is a large spread in the

Table 3. Summary of Analyses of September 23 SAR Images

Area Location (SAR Images 1,2, and 3, From Top to Bottom in Figures 4 and 10)	Features Observed in the Different Areas	Waves Obtained From SIPS	SWA-CMOD4 Wind Speed Comparison (Magnitude of Difference in the Area)	Wind Direction		
				SWA Combined With CMOD4	Hindcast	In Situ
Area 1, all open ocean sub-images in image 1	Some undefined brighter areas	Near azimuth propagating mode (about 250 m)	SWA< CMOD4 (0 to 1 m/s)	260°	250°	
Area 2, north-east of front	Some windrows (near the coast) that disappear in the area bounded by the front	Short mode of 75 m in near range direction and a weak strong mode of 200 m about 45° to range direction	SWA< CMOD4 (0 - 4 m/s)	305°	262°	260°
			closer to front: SWA>CMOD (1 - 2 m/s)	277°	266°	
Area 3, south of front	Windrows	Short mode of 75 m in near range direction and a strong mode of 200 m about 45° to range direction	SWA >CMOD4 (2 -6 m/s)	265°	261°	

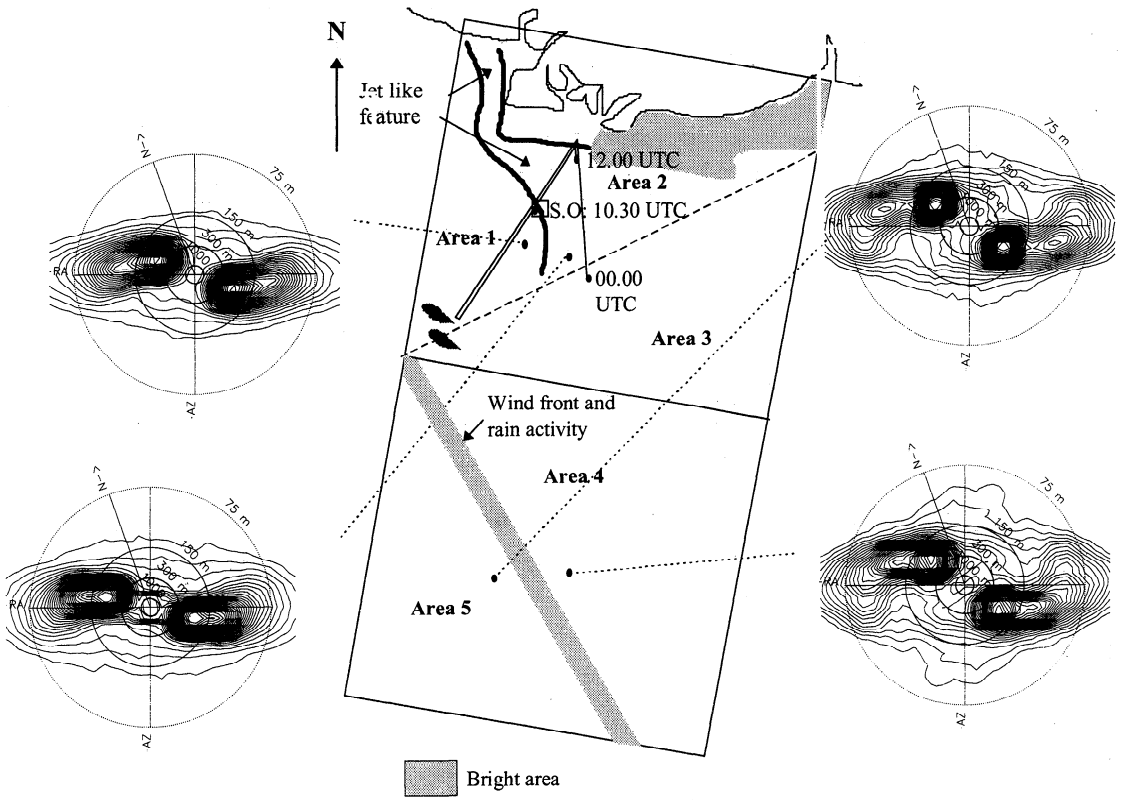

Figure 13. Identification of subareas of the SAR images on September 27, 1995 (center) together with the ship track prior to and during satellite overpass. The gray area marks the presence of windrows, and the lines roughly indicate the orientation but not the spacing of the windrows. The ship position at satellite overpass marked S.O. A selection of SAR image power spectra in the different areas is shown at left and right. The concentric circles indicate wavelengths of 1000 m (inner ring), 300, 150, and 75 m, RA is range direction, AZ is azimuth direction, and N is north.

SWA-derived wind speed for the areas. However, no evidence of wind shifts is found across the fronts.

From the SIPS analysis, a strong peak in the energy occurs between 150 and 300 m wavelength, 30° to 50° to the range axis. This peak in the SIPS is most likely caused by a corresponding peak in the real ocean wave spectrum, suggesting the presence of incoming swell. As proposed previously, the swell seems to strongly affect the wind field results, in particular, the SWA wind speed and the directional estimates.

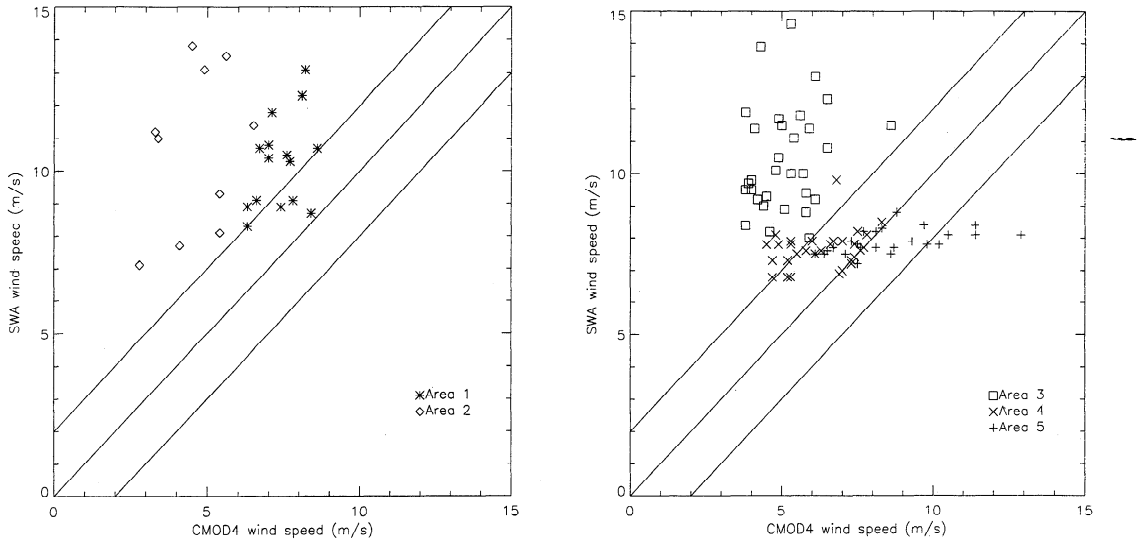

Figure 14. CMOD4 wind speed versus SWA wind speed derived from the SAR images on September 23, 1995. The interval of ±2 m/s is indicated.

Table 4. Summary of Analyses of September 27 SAR Images

Area Location (SAR Images 1,2, and 3, From Top to Bottom in Figures 2 and 6)	Features Observed in the Different Areas	Waves Obtained From SIPS	SWA-CMOD4 Wind Speed Comparison (Magnitude of Difference in the Area)	Wind Direction		
				SWA Combined With CMOD4	Hindcast	In Situ
Area 1, west of the jet feature in the first image	Uniform area some dark patches	200 m mode traveling about 30° relative to range direction	SWA>CMOD4 (4 to 7 m/s)			220°
Area 2,inside the jet feature in the first image	Bright patches	150 to 200 m mode traveling about 15° to 30° relative to range direction	SWA>CMOD4 (3 to 11 m/s)			260°
Area 3, south-east of diagonal in the first image	Uniform area	about 150 m mode traveling about 15° relative to range direction	SWA>CMOD4 (4 to 12 m/s)		205°	
Area 4, north-east of diagonal in the second image	Uniform area	150 to 200° traveling about 15° to 30° relative to range direction	SWA>CMOD4 (4 to 8 m/s)		220°	
Area 5, south-west of diagonal in the second image	Some bright spots (rain cells)	Strong 200 m mode traveling 45° relative to range axis	SWA>CMOD4 (4 to 8 m/s)	206°	219°	

Because of the large deviation in the SWA and CMOD4 wind speed, the retrievals of wind directions and in turn, wind vectors were possible only from area 5.

Table 4 summarizes the observations for the five areas analyzed in case 3 including a brief characterization of areas, features, SIPS results and the derived SWA versus CMOD4 wind speed differences, as well as comparisons of the wind direction retrievals. In comparison to the previous results, in particular from case 1, the results are poor. The SWA is consistently larger than CMOD4 by at least 4 m/s and completely without any correlation for the conditions encountered in case 3.

The boundary layer conditions prior to and during SAR acquisition observed from the R/*V Håkon Mosby* reveal a complicated and variable pattern in both time and space. During the ERS-1 overpass, the ship is located at the edge of the SST front. The measured wind speed varies from 3 to 10 m/s and is about 9 m/s at the time of satellite overpass. There is also a rapid variation in wind direction from 150° to 300° with a direction of approximately 220° at the satellite overpass. The observed air-sea temperature difference of about -1.5°C gave unstable ABL stratification west of the jet, while the air-sea temperature difference appears to be small (neutral ABL stratification) inside the jet. Under moderate wind speed, these gentle changes in stratification can cause a shift in the surface roughness, which is expressed by the SAR.

4. Discussion of Results

Table 5 provides the available in situ measurements as taken from the R/V *Håkon Mosby* and the buoy (for case 1) and corresponding SAR measurements taken from a SAR 10 × 10 km^2 subimage centered at the position of the R/V *Håkon Mosby* using the geographical corner and center coordinates provided with the SAR image and global positioning system (GPS) records from the ship. The database has also been enlarged, exceeding the number of SAR images in the case studies to include 10 SAR images where corresponding in situ measurements were available. In evaluating the result of this comparison, it should be noted that the two SAR wind speed retrieval methods are based on spatial averaging 10 × 10 km^2, while the in situ measurements represent 15 min temporal averages prior to SAR acquisition (corresponding to a 9 km travel distance at a speed of 10 m/s). In all cases, it is seen that the estimated wind speeds from the SWA and CMOD4 agree to within 2 m/s except on September 27. On the other hand, all cases show that the SAR-derived wind speeds are generally lower than the directly measured wind speed.

Table 6 summarizes the obtained wind direction as given in Tables 1-4 compared to the sparse number of in situ measurements and the available hindcast wind directions within the SAR frames. Table 6 reveals good agreement between the estimated wind directions and the in situ and modeled results. A deviance of less than 30° is obtained.

On September 16, when the ship was in the same position as the buoy at the satellite overpass, the wind speeds obtained from the SAR images (case 1) are 4 to 5 m/s lower than the in situ buoy- and ship-measured winds. Almost the same results are obtained when the SAR-derived and ship-measured wind speeds are compared on September 17. In contrast, the SAR-derived wind speeds from the area close to the buoy are in very good agreement with the in situ measurements. The SAR images for these 2 days had in common clear expressions of large areas of homogeneous windrows.

Table 5. Wind Speeds Obtained From SAR Images and In Situ Measurements From the R/V *Håkon Mosby* (H.M.) and the "Metocean" Buoy

Location of In Situ Measurement	Date in 1995	Estimated Wind Speed From SAR Image m/s		In Situ Wind Speed at Overpass (± 2 m/s)	Deviations (Absolute Value) m/s		
		SWA	CMOD4		SWA - CMOD4	In Situ- SWA	In Situ - CMOD4
H.M	Sept. 16	8	8	13	0	5	5
Buoy	Sept. 16	8	8	12	0	4	4
H.M.	Sept. 17	4	3	5	1	1	2
Buoy	Sept. 17	9	10	10	1	1	0
H. M.	Sept. 23	5	6	12	1	7	6
H. M.	Sept. 22	6	8	12	2	6	4
H. M.	Sept. 14	5	4	6	1	1	2
H. M.	Sept. 26	9	7	14	2	5	7
H. M., (ERS-1)	Sept. 27	9	5	6	4	3	1
H. M., (ERS-2)	Sept. 27	10	4	10	6	0	6
Deviation (Mean)					1.8	3.3	3.7

In case 2 on September 23, the deviations in the SWA and CMOD4 retrievals and the in situ measured wind speed have increased to 6-7 m/s, while the SWA wind speed compares well with the in situ ship measurement in case 3 on September 27. In this latter case the CMOD4 wind speed is far too low. Overall, the magnitude of the in situ measured wind speed in the region remains from 10 to 13 m/s (except for September 17) for these three cases and cannot therefore explain the wide span that results from comparison with the SAR-derived winds. On the other hand, the SAR images from the two days in cases 2 and 3 have in common an increase in spatial variability in backscatter at the expense of clear expressions of homogeneous windrow areas. The effect of this on the wind and wave field retrievals from the SAR images may cause the larger discrepancies.

On average, Table 5 shows that the mean deviation of the two SAR wind speed retrieval methods is less than 1.8 m/s, and grows to 3.3 m/s and 3.7 m/s for the in situ SWA and the in situ CMOD4 wind speeds, respectively. Regarding the wind direction retrievals, on the other hand, there is a good overall agreement, except for the case 3 on September 27 and the additional SAR scene from the same date. Again, we emphasize that this is locally in the position of the in situ measurements and does not reveal the spatial variability.

Although the two SAR retrieval methods agree quite well, as demonstrated in the previous section and summarized in Table 5, several possible effects and error sources in the CMOD4 and SWA wind field retrievals may explain the wide range of results when locally compared to in situ measurements as suggested in Table 7. This may also explain some of the spatial variability we obtain in comparing the SWA and the CMOD4 results in cases 1 to 3. In the following, some of these are considered in more detail, without reflecting on possible uncertainties and errors from the in situ measurements.

As mentioned above, fetch-limited seas can lead to underestimation of the local SWA wind retrievals since the sea state has not reached equilibrium with the local wind speed [*Kerbaol et al.*, 1996; *Korsbakken and Johannessen*, 1996]. This effect can be compensated for, provided the wind direction and fetch distance can be determined. This effect may explain the deviation between the SWA and in situ measurements for case 1, September 16 and 17 SAR images, where we expect fetch-limited seas at least in the northern parts of the images. The fetch dependency is theoretically estimated by *Kerboal* [this issue] for fetch of 50, 100, and 200 km. The azimuth cutoff wavelength decays as a function of the wind speed at different fetch compared to a fully developed sea. The corresponding underestimation of wind speed in SWA becomes significant at 10 m/s wind speed if the seas are not fully developed. An approximate correction for our results in case 1 is estimated if the fetch is assumed to have the following characteristics: (1) 50 to 100 km in the position of in situ measurements (Figure 2 and Table 5) on September 16,

Table 6. Wind Directions Obtained From SAR Images and In Situ Measurements From the R/V *Håkon Mosby* (H.M.), "Metocean" Buoy and Hindcast Data

Date in 1995	Estimated Wind Direction From SAR Image.	In Situ Wind Speed Direction at Overpass H. M. or Buoy	Nearest Available Hindcast Data	Deviations (Absolute Value) Wind From SAR	
				In Situ	Hindcast
Sept. 16	84	-	114		30
	105	-	152		47
	125	-	124		1
	136	130	114	6	22
	96	-	123		27
Sept. 17	98	-	124		26
	108	-	147		39
	101	100	124	24	23
	100	-	107		7
	87	-	96		9
	140	-	101		39
Sept. 23	260	-	250		10
	305	-	262		43
	277	260	266	6	11
Sept. 27	206		219		13
Deviation (Mean)				12	23

All numbers except dates in degrees.

and the correction in wind speed 1 to 3 m/s; (2) 50 km in the ship position (Figure 3) on September 17, yielding a correction of 1 m/s; and (3) 100 km in the buoy position (Figure 3) on September 17, yielding a correction of 1 m/s. Adding these corrections to the SWA wind speed will reduce the difference between the SWA wind speeds and in situ measurements.

In contrast, incoming swell generated by surface winds outside the region will, of course, introduce a surface wave field that is not, again, directly in equilibrium with the local wind field. Hence, the SWA method might overestimate the local wind speed because of increased smearing.

The CMOD4 wind speed estimates appear not to be affected by fetch-limited seas. Instead, this method is affected by surface boundary layer conditions such as the stratification and presence of surface films. While the former effect can be corrected for via a boundary layer model for stable (intensify wind speed at 10 m) or unstable (reduce wind speed at 10 m) stratification [e.g. *Wu* 1993], the effect of the latter will always dampen the surface roughness and hence reduce the wind speed. Assuming the weakly unstable (-1.0 to -2.0°C) boundary layer stratification reported from the ship to be valid across the entire images, the CMOD4 wind speed at 10 m above the surface will be reduced. At the same time an increased presence of film due to accumulation of breaking air bubbles returning to the surface after the wind maximum passed early on September 16 will further magnify this reduction. Quantifying here is difficult because the attenuation of σ_0 depends on the unknown thickness of the surface films.

An uncertainty factor in applying the CMOD4 model to SAR data is local variations in the surface wind direction and, in turn, our assumption of a local in situ measurement to be valid in all subimages in the imaged area. The only confidence in this assumption applies to case 1, where windrows confirm the homogeneity of the wind direction. The variability in wind speed due to variations in the wind direction is illustrated in Figure 15 for examples of 5 m/s and 15 m/s CMOD4 wind speed. Deviance in CMOD4 wind speed due to error in the wind direction used, as taken from in situ measurements or windrows in SAR images, is plotted for variations around 0°, 45°, and 90° wind direction (relative to the satellite look direction). Because of the wind-directional asymmetry in the

Table 7. Overview of Observed Problems and Possible Explanations for the Case Studies

Date in 1995	Observed Problem	Possible Explanation(s)
16 September	SWA wind speeds lower than in situ measurements	Fetch limited seas
	CMOD4 wind speed lower than in situ measurements	Local variations in wind direction; surface films
17 September	SWA wind speeds lower than in situ measurements	Fetch limited seas
	CMOD4 wind speeds lower than in situ measurements	Variations in wind direction
23 September	SWA wind speed generally higher than CMOD4 wind speed	Incoming swell (increase in SWA); all effects reducing CMOD4 wind speed
27 September	SWA wind speed generally higher than CMOD4 wind speed	Incoming swell
	CMOD4 wind speed less than in situ wind speed	Stratification; variations in wind direction

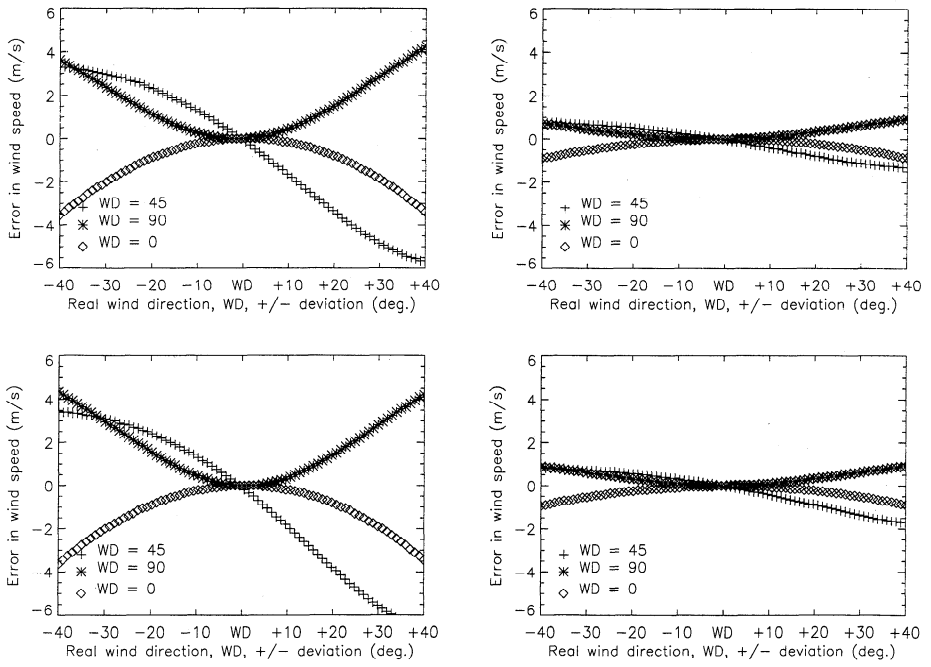

Figure 15. The error in the estimated CMOD4 wind speed due to deviations in the wind direction. Upper left plot is for a wind speed of 15 m/s for 0°, 45°, and 90° wind direction (WD) and WD ± 0° to 40° relative to the satellite look direction; the incidence angle is 20°. Upper right is a similar plot for a wind speed of 5 m/s at 20° incidence angle. At WD the error in wind speed is 0 m/s. Lower left and right plots follow the same pattern as the upper left and right plots except for the incidence angle, which is changed to 26°.

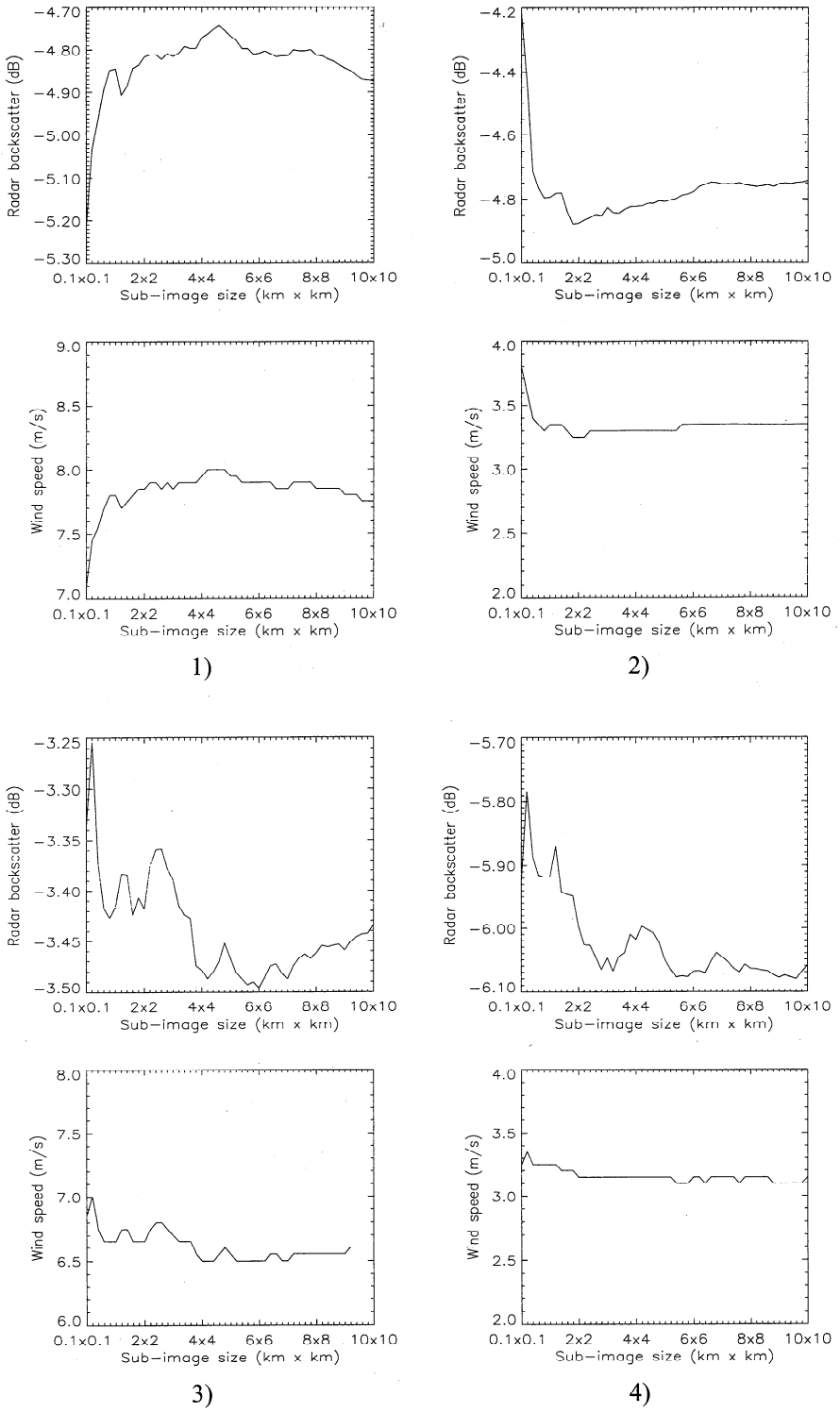

Figure 16. Plots of the σ_0 and corresponding CMOD4 wind speed measurement as a function of subimage size. Plots 1 and 2 are taken from the same position as the in situ measurements from the R/V *Håkon Mosby* in case 1 on September 16 and 17. Plots 3 and 4 corresponds to in-situ measurements in case 2 and 3 on September 23 and 27, respectively.

CMOD4 model, the largest errors occur, if the used wind direction has positive deviations from a real wind direction of 45°. Figure 15 also shows that the error estimate does not vary in the range of ERS SAR incidence angles of about 19° to 26°. For the relatively high wind speeds observed in most of the cases in this study, the wind direction used to derive the CMOD4 wind speed becomes a significant error source and may cause errors up to 5 m/s in the derived wind speed.

In comparing the CMOD4 and in situ measurements, we do not obtain as good quantitative agreement as *Vachon and Dobson* [1996] in their comparison to in situ measurements. The discrepancy between our CMOD4 results and the results

obtained by *Vachon and Dobson* [1996] seems to be difficult to explain and has to be further investigated. In this work the spatial resolution of the CMOD4 estimates was primarily chosen to be the same as the spatial resolution for the SWA method, which in turn, may explain the better agreement when comparing SWA and CMOD4 wind speed retrievals than when comparing CMOD4 and local in situ measurement. *Vachon and Dobson* [1996] used a subimage size of 4×4 km. However, choosing this same size of the subimage did not significantly improve the agreement with in situ measurements in our case, as illustrated in Figure 16, which shows the variability in σ_0 and the corresponding CMOD4 wind speed as a function of increasing the subimage from 100×100 m to 10×10 km. The enlargement of the subimages is done symmetrically around the location of the in situ measurements from the R/V *Håkon Mosby*. In general, the plots in Figure 16 show small variations in σ_0 as a function of the subimage size and the corresponding CMOD4 winds do not change significantly in any of the cases.

Moreover, the CMOD4 is capable of quantifying the change in wind speed and direction across wind fronts. The radar backscatter will have a maximum change, if for a given wind speed change the wind direction at the same time changes from the near range in the high wind zone to the near azimuth on the low wind side of the front [*Johannessen et al.*, 1991].

In summary, the performances of the two SAR wind retrieval methods are best for case 1 on September 16 and 17. Images for these days are similar with respect to the meteorological situation, the windrows in the SAR images and the SIPS. Gradual spatial variations in both the SWA and CMOD4 wind speeds over several subimages (considered as independent samples) therefore give confidence in the wind speed estimates, assuming that the wind and wave field undergoes small changes at a scale similar to the subimage.

5. Summary

In this paper we have shown that the radar backscatter and spectral signatures of the ocean surface obtained from ERS-1 and 2 SAR images can provide valuable and quantitative information on near-surface wind speed and wind direction. Ten ERS SAR images, from September 16,17, 23, and 27, 1995 have been examined by studying their σ_0 and spectral properties in 736 subimages. Two different wind retrieval models, SWA and CMOD4, have been applied to the data. We have found by comparing the SWA and CMOD4 wind speed retrievals that 65% of the sub images gives a wind speed difference less than 2 m/s, but the comparison also reveals relatively large spatial variations in the agreement due to different scattering clusters. In general, we also obtain an underestimation of the wind speed from SAR in comparison with the available in situ observations. The obtained wind directions are also in good agreement with the hindcast results and in situ measurements and are consistent with the good agreement in wind speed. However, we also observe diverging results in specific areas.

It is demonstrated that the surface conditions impact on the performances of the different wind field retrieval methods and their corresponding results. The presence of homogeneous windrows is clearly favored. For fetch-limited seas and in vicinity of wind fronts, on the other hand, the SWA method underestimates the wind speed. For fetch-limited seas the waves are not in equilibrium with the near-surface wind speed. Hence the distribution of the velocity field of surface scatters, as introduced by the orbital velocity of the waves, will be narrower than for fully developed seas, leading to underestimation. Moreover, the relatively large relaxation rate for the longer wind waves (also the medium wavelengths suppressed by the general resolution of the SAR) allows these waves to propagate across a wind front. Hence they will maintain their original equilibrium state over some distance away from the front. In turn, the wind front will not be resolved properly by the SWA method. For the same reason, the presence of swell may cause an increase in the derived wind speed. In contrast, the CMOD4 method is not limited by these conditions.

While absolute image calibration is necessary for the CMOD4 method, it is not required for the SWA method, since the former method uses radar backscatter values while the latter uses spectral characteristics. However, as mentioned in the analysis of the September 17 image, the SWA method is limited to SAR images containing clear wave modulation from which the azimuth cutoff can be derived. In the case of very low wind conditions (lower than approximately 3 m/s) or in the presence of slicks, the SWA method will therefore break down, but these conditions will also affect the CMOD4, since the threshold wind speed for C band waves is around 3 m/s [*Johannessen et al.*, 1996].

Further investigation of these methods is necessary in order to fully understand their limitations and strengths, particularly in regard to the surface conditions and synoptic weather situation. However, as reported in this and other papers on wind retrievals from SAR (included in this special section), the possibility looks promising in regard to the continuation of regular spaceborne SAR observations.

Acknowledgments. This work was funded by the Norwegian Research Council as a part of a strategic SAR program at the Nansen Environmental and Remote Sensing Center. The SAR data were provided under the ESA AO2/N108 (announcement of opportunity) program. The ship time for the Coast Watch'95 experiment was provided and funded by the University of Bergen. The following contributions are highly appreciated: Ken Davidson and Paul Fredrickson at the Naval Postgraduate School for providing the buoy measurements and Magnar Reistad at the Norwegian Meteorological Institute for providing the weather diagnostics.

References

Chapron, B., T. E. Fouhaily and V. Kerbaol, Calibration and validation of ERS wave mode products, *Doc. DRO/OS/95-02*, Inst. Fr. de Rech. pour l'Exploit. de la Mer, Brest, France, 1995.

Hasselmann, K. and O.H Shemdin, Remote Sensing Experiment Marsen, *Int. J. Remote Sens.*, 3, 139 - 361, 1982.

Johannessen, J.A., R. Shuchman, O. M. Johannessen , K. Davidson and D. R. Lyzenga, Synthetic aperture radar imaging of ocean circulation features and wind fronts, *J. Geophys. Res.*, *96*, 10,411-10,422, 1991.

Johannessen, J.A., P.W. Vachon and O.M. Johannessen, ERS-1 SAR imaging of marine boundary layer processes, *Earth Observation Quarterly*, European Space Agency, Paris, France, 1995.

Johannessen, O. M. et al., Coast Watch'95 ERS-1,2 SAR applications of mesoscale upper ocean and atmospheric boundary layer processes off the coast of Norway, paper presented at IGARSS'96, Int. Geosci. and Remote Sens. Symp., Lincoln, Nebr., 1996.

Kerbaol, V., B. Chapron, T. El Fouhaily, and R. Garello, Fetch and wind dependence of SAR azimuth cutoff and higher order statistics in a mistral case, paper presented at IGARSS'96, Int. Geosci. and Remote Sens. Symp., Lincoln, Nebr., 1996.

Kerbaol, V., B. Chapron, and P. W. Vachon, Analysis of ERS-1/2 synthetic aperture radar wave mode imagettes, *J. Geophys. Res.*, this issue

Komen, G. J., L. Cavaleri, M. Donelan, K. Hasselmann, S. Hasselmann, K. Davidson and P.A.E.M Janssen, *Dynamics and Modelling of Ocean Waves,* Cambridge Univ. Press, Cambridge, 1994.

Korsbakken, E,. Quantitative wind field retrievals from ERS SAR images, Young graduate trainee report, Ocean and Sea Ice Unit, Earth Sci. Div., Eur. Space Res. and Technol. Cent., Eur. Space Agency, Noordwijk, The Netherlands, 1996.

Korsbakken, E and J. A. Johannessen, Quantitative wind field retrievals from ERS SAR images, paper presented at the Third ERS Workshop, Inst. Fr. de Rech. pour l'Exploit. de la Mer, Brest, France, June 18-20, 1996.

Laur, H., P. Meadows, J. I. Sanchez and E. Dwyer, ERS-1 radiometric calibration, technical report, Eur. Space Res. Inst., Frascati, Italy, 1993.

Laur, H., P. Bally, P. Meadows, P. J. Sanchez, B. Schaettler, E. Lopinto, Derivation of the backscattering coefficient σ_0 in ESA ERS SAR PRI products, Doc. *ES-TN-RS-PM-HL09*, issue 2, rev. 2, Eur. Space Res. Inst., Frascati, Italy, June 28, 1996.

Meadows, P. J. and C. J Willis, Derivation of radar cross section coefficient in UK-PAF ERS-1.SAR.PRI products, GEC-MARCONI Res. Cent, Chelmsford, Essex, 1995.

Monaldo, F. M., The consequences of sampling variability on the estimation of wave number and propagation direction from spaceborne SAR image spectra, *IEEE Trans. Geosci. Remote Sens., 29* (1), 113-119, 1991.

Scoon, A., T. S. Robinson, and P. J. Meadows, Demonstration of an improved calibration scheme for ERS-1 SAR imagery using a scatterometer wind model, *Int. J. Remote Sens., 17* (2), 413-418, 1996.

Smith, D. S., Coefficients for sea surface wind stress, heat flux, and wind profiles as a function of wind speed and temperature, *J. Geophys. Res., 93,* 15,467-15,472, 1988.

Stoffelen, A. and D.L.T. Anderson, ERS-1 scatterometer data and characteristics and wind retrieval skills, Proceeding of First ERS-1 Symposium, *Eur. Space Agency Spec. Publ., ESA SP-359*, 1993.

Vachon, P.W, and F.W Dobson, Validation of wind vector retrieval from ERS-1 SAR images over the ocean, *The Global Atm. and Ocean Sys.*, 5, 177-187, 1996.

Vachon, P.W., H. E. Krogstad, and J. S. Paterson, Airborne and spaceborne synthetic aperture radar observations of ocean waves, *Atmos.-Ocean 32*, 83-112, 1994.

Vachon, P.W., J.A Johannessen, and D. P Browne, ERS-1 SAR images of atmospheric gravity waves, *IEEE Trans. Geosci. Remote Sens., 33* (4), 1014-1025, 1995.

Wakerman, C.C, C. L. Rufenach, R. Shuchman, J. A. Johannessen, and K. Davidson, Wind vector retrieval using ERS-1 synthetic aperture radar imagery, *IEEE Trans. Geosci. Remote Sens.*, 34, 1343-1352, 1996.

Wu, J., Ripples and oceanic remote sensing, in *Proceedings Environment'93,* The Hong Kong Univ. of Sci. and Technol., The Commercial Press Ltd., Hong Kong, 1993.

J. A. Johannessen, ESA-ESTEC, P.O. Box 299, 2200 AG Noordwijk, The Netherlands. (email: jjohnne@estec.esa.nl)

O. M. Johannessen and E. Korsbakken, Nansen Environmental and Remote Sensing Center, Edv. Griegs Vei 3A, N-5037 Solheimsviken, Bergen, Norway. (email: ola.johannessen@nrsc.no; erik.korsbakken@nrsc.no)

(Received March 18, 1997; revised August 25, 1997;
accepted September 8, 1997.)